Journal of Instrumentation

OPEN ACCESS

Front-side biasing of n-in-p silicon strip detectors

To cite this article: M. Baselga *et al* 2018 *JINST* **13** P11007

View the article online for updates and enhancements.

IOP ebooks™

Bringing you innovative digital publishing with leading voices to create your essential collection of books in STEM research.

Start exploring the collection - download the first chapter of every title for free.

This content was downloaded from IP address 141.52.96.80 on 31/05/2019 at 11:03

Jinst

PUBLISHED BY IOP PUBLISHING FOR SISSA MEDIALAB

RECEIVED: *May 9, 2018*
REVISED: *September 14, 2018*
ACCEPTED: *October 30, 2018*
PUBLISHED: *November 8, 2018*

2018 JINST 13 P11007

Front-side biasing of n-in-p silicon strip detectors

M. Baselga,[a] T. Bergauer,[b] A. Dierlamm,[a] M. Dragicevic,[b] A. König,[b] M. Metzler[a,1] and E. Pree[b]

[a] *ETP (KIT), Hermann-von-Helmholtz-Platz 1, 76344 Eggenstein-Leopoldshafen, Germany*
[b] *HEPHY, Nikolsdorfer Gasse 18, 1050 Wien, Austria*

E-mail: marius.metzler@kit.edu

ABSTRACT: Front-side biasing is an alternative method to bias a silicon sensor. Instead of directly applying high voltage to the backside, one can exploit the conductive properties of the edge region to bias a detector exclusively via front-side connections. This option can be beneficial for the detector design and might help to facilitate the assembly process of modules. The effective bias voltage is affected by the resistance of the edge region and the sensor current. The measurements of n-in-p sensors performed to qualify this concept have shown that the voltage drop emerging from this resistance is negligible before irradiation. After irradiation, however, the resistivity of the edge region increases with fluence and saturates in the region of $10^7\,\Omega$cm at fluences above $6 \cdot 10^{14}\,\mathrm{n_{eq}cm^{-2}}$ and an operation temperature of $-20\,°$C. The measurements are complemented by TCAD simulations and interpretations of the observed effects.

KEYWORDS: Radiation-hard detectors; Si microstrip and pad detectors

[1] Corresponding author.

© 2018 The Author(s). Published by IOP Publishing Ltd on behalf of Sissa Medialab. Original content from this work may be used under the terms of the Creative Commons Attribution 3.0 licence. Any further distribution of this work must maintain attribution to the author(s) and the title of the work, journal citation and DOI.

https://doi.org/10.1088/1748-0221/13/11/P11007

Contents

1 Introduction 1

2 Experimental setup and simulation environment 2

3 Resistivity 4

4 Characteristic measurements on unirradiated sensors 5

5 Impact of edge dimensions 8

6 Bias voltage dependency 9

7 Temperature dependence before irradiation 11

8 Impact of irradiation 13

9 Annealing effects 17

10 Extrapolation to large sensors 18

11 Summary 19

2018 JINST 13 P11007

1 Introduction

Large silicon tracking devices, as they are used in modern high energy physics (HEP) experiments such as CMS, ATLAS or LHCb at the Large Hadron Collider (LHC), are composed of thousands of stand-alone units. These units are called modules and consist of one or multiple silicon sensors, front-end electronics, as well as support structures.

The conventional biasing scheme of a silicon strip sensor uses a ground connection on the front-side while a high voltage (HV) connection is applied to the backside (backside biasing: BSB). The HV connection is attached, glued and wire-bonded to the backside and the wire bonds must be encapsulated. Building a reliable connection is a complicated task. Moreover, placing a sensor face down on the bonding support to be able to process the backside can be a risky operation. Front-side biasing (FSB) is an alternative method to bias a silicon sensor that was introduced in ref. [1]. By applying HV to the front-side close to the edge region, one can utilize the conductive characteristic of the sensor edge to interconnects front to back-side. This approach would eliminate risky and time-consuming assembly steps and facilitate the module construction.

This study was performed in the framework of the CMS Phase-2 Tracker Upgrade. However, the study investigates the validity of front-side biasing for modern HEP experiments in general. Characteristic measurements on small strip sensors (referred to as mini sensors in this paper) are

Table 1. List of sensors used in this study. The sensor nomenclature indicates the sensor design (first character) and the active sensor thickness in microns (digits). The D sensors were produced by IFX and are made of thinned float-zone material. All other samples were produced by HPK and are made of deep-diffused material with a physical thickness of 320 µm.

Sensor name	A_{sensor} (cm^2)	A_{edge} (cm^2)
A200	1.83	0.38
A240	1.83	0.38
B200	3.10	0.46
B240	3.10	0.46
C240	6.96	0.81
X240	96.66	2.54
D200	13.49	1.01

compared under front-side-biased and back-side-biased modes of operation. Furthermore, the edge resistivity and its dependence on temperature, fluence, and bias voltage is studied by evaluating experimental, theoretical, and simulated data. Eventually, the measured resistivities can be used to approximate the voltage drop and additional power consumption of a large front-side-biased silicon sensor before and after irradiation.

2 Experimental setup and simulation environment

Table 1 lists the samples that were used in this study, and their edge areas and full surface areas, A_{edge} and A_{sensor}. The definition of A_{edge}, as well as a detailed description of sensor specific terms and design details, can be found in section 4. The corresponding detector wafers were fabricated by two different vendors. The sensors were produced with similar masks and designs, using different silicon materials. The wafers manufactured by HPK [2] are composed of deep-diffused[1] float-zone (ddFZ) silicon with a physical thickness of 320 µm. These samples have an active thickness of either 240 µm or 200 µm. The wafers processed by IFX [3] are made of float-zone silicon (FZ) that is physically thinned to 200 µm. The bulk material of all samples is p-doped silicon while the strip and bias ring implants are n-doped [4], referred to as n-in-p. The edge implant on the front-side as well as the backplane implant are p-doped. The doping concentration of the p-bulk is approximately $N = 10^{12}\,\text{cm}^{-3}$, while the value for strip, backside and edge implants is about $N = 10^{19}\,\text{cm}^{-3}$.

The edge resistivity measurements were performed in custom-made probe station setups at ETP (KIT) [5, 6] and HEPHY [7]. These setups provide temperature control and allow a sensor biasing up to full depletion or higher. To achieve bulk depletion while measuring the edge resistance at the same time, one has to utilize the measurement scheme presented in figure 1 using two source measurement units (SMUs). The backplane is set to ground potential and acts as a common reference point for both units. In order to deplete an n-in-p sensor, the n-doped implants need to be set to a higher potential than the p-doped bulk. The first SMU is therefore used to apply a positive

[1]Deep-diffusion reduces the active thickness of the material by diffusing dopants from a highly doped backside implant further into the wafer bulk. This technology is intellectual property of HPK.

2018 JINST 13 P11007

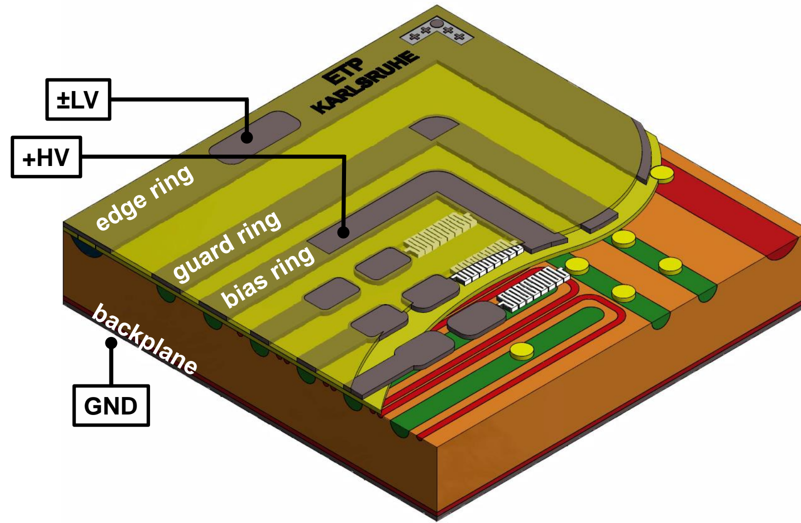

Figure 1. 3D sketch of the corner region of a standard strip sensor, which incorporates the scheme of an edge resistivity measurement. Voltage ramps are performed between edge ring and backplane to obtain the resulting current through the edge region. The backplane is grounded to create a common reference point (GND). The bias ring is set to a positive high voltage (HV). The edge ring can be set to either positive or negative low voltage potential (LV).

high voltage to the bias ring and to measure the sensor's leakage current. An additional low voltage (LV) offset between backplane and edge region is realized by a second SMU, which measures the edge current.

Simulations were carried out with the Synopsys Sentaurus TCAD [8] toolkit, a simulation package for semiconductors using the finite element method. Different geometries and parameters were used for the simulations, in order to confirm the experimental results. Most simulations were carried out with a simplified geometry of D200 and B240 (table 1), which includes an extra wide bias ring instead of a bias ring and strips. This has proven to be a valid approximation, since the edge region is the major focus here and the results only differed by a negligible amount ($< 1\%$ difference for simulated edge currents of simplified and full geometry). The interface charge density between the silicon bulk and the silicon dioxide layer, N_{ox}, which is present in the edge region, is $10^{11}\,\mathrm{cm}^{-2}$ for HPK sensors. According to ref. [9], N_{ox} is about $2 \cdot 10^{10}\,\mathrm{cm}^{-2}$ for unirradiated IFX sensors, which is incorporated into the simulations. The radiation damage model which was used is presented in ref. [10]. The corresponding defect parameters of the simulations are listed in table 2. The model is valid for fluences between $1 \cdot 10^{14}\,\mathrm{n_{eq}cm^{-2}}$ and $1 \cdot 10^{15}\,\mathrm{n_{eq}cm^{-2}}$. It postulates a constant number of positive interface oxide charges $N_{ox} = 1 \cdot 10^{12}\,\mathrm{cm}^{-2}$ for proton irradiation.

Irradiations for this study were carried out with 23 MeV protons at ZAG [11]. Fluences in the unit of 1 MeV neutron equivalent per cm ($\mathrm{n_{eq}cm^{-2}}$) ranged from $1 \cdot 10^{13}\,\mathrm{n_{eq}cm^{-2}}$ up to $2 \cdot 10^{15}\,\mathrm{n_{eq}cm^{-2}}$. The fluences for strip tracking detectors at the HL-LHC are expected to range from $3 \cdot 10^{14}\,\mathrm{n_{eq}cm^{-2}}$ to $1 \cdot 10^{15}\,\mathrm{n_{eq}cm^{-2}}$ for $3000\,\mathrm{fb^{-1}}$ [12]. This depends on the geometry of the tracking device, the distance from the vertex and the position of a particular module layer.

2018 JINST 13 P11007

Table 2. Parameters of the irradiation model [10] used for TCAD simulations, using one donor and acceptor defect. The energy is given with respect to the valence band energy E_V and the conduction band energy E_C. The concentration is assumed to be proportional to the fluence Φ. The parameters σ(e) and σ(h) denote the electron and hole cross section of those defects.

Parameter	Donor	Acceptor
Energy (eV)	$E_V + 0.48$	$E_C - 0.525$
Conc. (cm^{-3})	$5.598\,\mathrm{cm}^{-1} \times \Phi - 3.949 \cdot 10^{14}$	$1.189\,\mathrm{cm}^{-1} \times \Phi + 6.454 \cdot 10^{13}$
σ(e) (cm^2)	$1.0 \cdot 10^{-14}$	$1.0 \cdot 10^{-14}$
σ(h) (cm^2)	$1.0 \cdot 10^{-14}$	$1.0 \cdot 10^{-14}$

3 Resistivity

The resistivity ρ, which is the inverse of the conductivity σ, can be expressed as a function of the electron charge q, the carrier densities p and n as well as the carrier mobilities μ_h and μ_e [13]:

$$\rho = \frac{1}{\sigma} = \frac{1}{q(n\mu_e + p\mu_h)} . \tag{3.1}$$

The intrinsic carrier density n_i can be written as a function of the effectively availible states in the conduction and valence band, N_c and N_v, in addition to the band gap energy E_g [13]:

$$n_i = \sqrt{N_v N_c}\,\exp\left(-\frac{E_g}{2kT}\right) . \tag{3.2}$$

From this equation one can derive the mass action law. It states that the product of p and n is constant:

$$np = n_i^2 . \tag{3.3}$$

The temperature dependence of n_i is determined by N_v and N_c. Higher states in the conduction and deeper states in the valence band become more accessible as the thermal energy increases. One finds that n_i is proportional to $T^{\frac{3}{2}}$ with c being a combination of constants:

$$n_i = 2(cT)^{\frac{3}{2}}\,\exp\left(-\frac{E_g}{2kT}\right) . \tag{3.4}$$

In doped semiconductors the free carrier density equals the doping conecentration. The resistivity formula can be written as a function of the effective doping concentration N_{eff}, which is defined by the difference between acceptor and donor concentration [14]:

$$\rho = \frac{1}{q\mu|N_{\text{eff}}|} . \tag{3.5}$$

Based on this formula, one can derive the relation between ρ, V_{fd}, the active sensor thickness, L, the electric field constant, ϵ_0 and the relative permittivity of silicon, ϵ_r:

$$\rho = \frac{L^2}{2\mu\epsilon_0\epsilon_r V_{\text{fd}}} . \tag{3.6}$$

2018 JINST 13 P11007

The temperature dependence of ρ in semi-conductors is explained in ref. [13]. The resistivity is a function of carrier mobility and density as shown in Equation (3.1), which are both functions of temperature. Dopants are completely ionized in a temperature range between roughly −170 °C and 130 °C (100 K and 300 K). Hence, the carrier density is determined by the doping concentration and is therefore constant. This is referred to as the extrinsic or saturation region [15–17]. Since this is the temperature region in which all measurements were performed, the carrier mobility becomes the determining factor. The total carrier mobility, μ_{t}, is a superposition of mainly two processes. As stated by Matthiessen's law, these two contributions are related to phonons and impurities:

$$\frac{1}{\mu_{\mathrm{t}}} = \frac{1}{\mu_{\mathrm{imp}}} + \frac{1}{\mu_{\mathrm{pho}}} . \tag{3.7}$$

At low temperatures the carrier mobility is dominated by the μ_{imp}-term. The process is driven by increasing ionization and impurity scattering. With increasing temperature phonon scattering begins to dominate, which leads to an inverted temperature dependency [13, 16]:

$$\mu_{\mathrm{imp}} \sim T^{\frac{3}{2}} , \tag{3.8}$$

$$\mu_{\mathrm{pho}} \sim T^{-\frac{3}{2}} . \tag{3.9}$$

The carrier mobilities of extrinsic silicon were measured in ref. [18] for a broad temperature spectrum and different impurity concentrations. Near room temperature the mobility is found to be proportional to $T^{-2.42}$ for a doping concentration $N \leq 10^{12}\,\mathrm{cm}^{-3}$, which equates to the expected N of the sensor bulks used in this study. The exponent $a = -2.42$ differs from the theoretically expected value of $a = -1.5$ in Equation (3.9) because of other scattering mechanisms [13]. As stated by Equation (3.1), resistivity is inversely proportional to carrier mobility, which yields the expected temperature dependency of ρ:

$$\rho \sim T^{2.42} . \tag{3.10}$$

If the resistance of a resistor and its dimensions are known, one can calculate the resistivity of the material using the resistor formula. Within the scope of this study, we determined the edge resistivity of silicon sensors knowing their precise dimensions. Therefore the formula can be written as follows:

$$\rho = R_{\mathrm{edge}} \cdot \frac{A_{\mathrm{edge}}}{L} , \tag{3.11}$$

where A_{edge} is the edge area and R_{edge} is the edge resistance. The length L is equal to the active not the physical thickness of the sensor. With a doping concentration of about $1 \cdot 10^{19}\,\mathrm{cm}^{-3}$ the resistivity of the highly doped, deep-diffused back-side layer is below 1 Ωcm and therefore several orders of magnitude smaller than the bulk resistivity [15].

4 Characteristic measurements on unirradiated sensors

The edge needs to be protected from high electric fields, which is realized by a heavily doped edge implantation on the front-side. The implantation in combination with the broad aluminum layer

2018 JINST 13 P11007

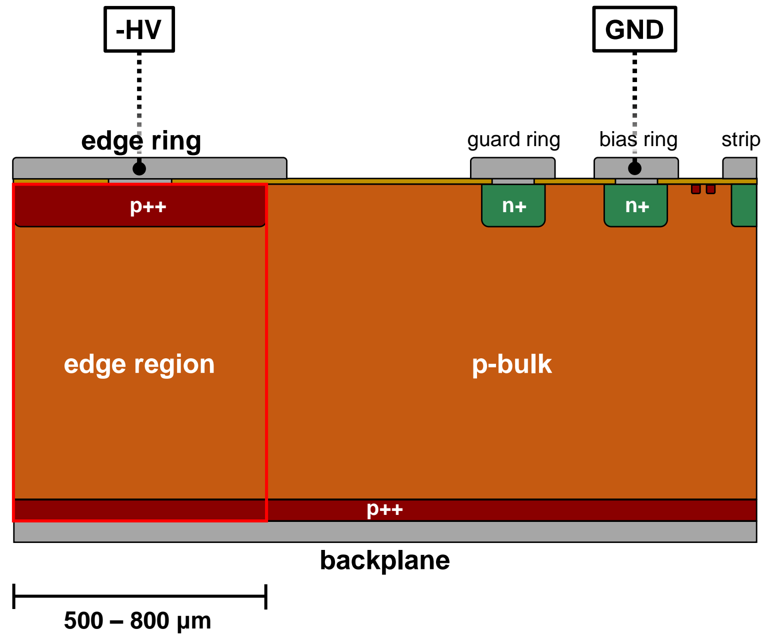

Figure 2. 2D sketch of an n-in-p strip sensor. It demonstrates the terminology used in this document and highlights the front-side biasing scheme. The bias ring is grounded while -HV is applied to the edge ring instead of the backplane (as it is the case for back-side biasing). Highly p-doped implants are located beneath the edge ring and on the bottom of the sensor bulk. Strip as well as guard and bias ring implants are n-doped. The red box highlights the region which we define as the edge.

right above is called the edge ring. It has several openings in the protective passivation layer for electrical contacting. The entire section below this aluminum ring is defined as the edge. The respective sensor regions are visualized and named in figure 2. The edge dimensions in addition to the material related resistivity, ρ, fully determine the edge resistance, R_{edge}. Our definition of the edge area, A_{edge}, is shown in figure 2. It is given by the sensor layout and can be calculated by adding up the area between cutting edge and inner border of the edge implant.

As an initial simple check on how the biasing schemes of FSB and BSB might differ one can measure the current-voltage (IV) and capacitance-voltage (CV) characteristics. For BSB the HV was applied to the back-side, while for FSB it was applied to the edge ring as depicted in figure 2. Respective plots are shown in figure 3 and 4 for two different samples of differing size. As shown in table 1, the driving factor in terms of difference in current and capacitance between C240 and B240 is the sensor area. A larger sensor area (volume) results in higher leakage current and capacitance at a given bias voltage. There is little observable difference between the FSB and BSB scheme. From this result one can conclude that the resistance of the sensor edge in this state must be very small, which results in a negligible voltage drop, ΔV, across the sensor edge. The effective bias voltage applied between the bulk and bias ring, V_{eff}, is therefore of the same value as the applied bias voltage, V_{bias}. These quantities relate as follows:

$$V_{\text{eff}} = V_{\text{bias}} - \Delta V \,. \tag{4.1}$$

2018 JINST 13 P11007

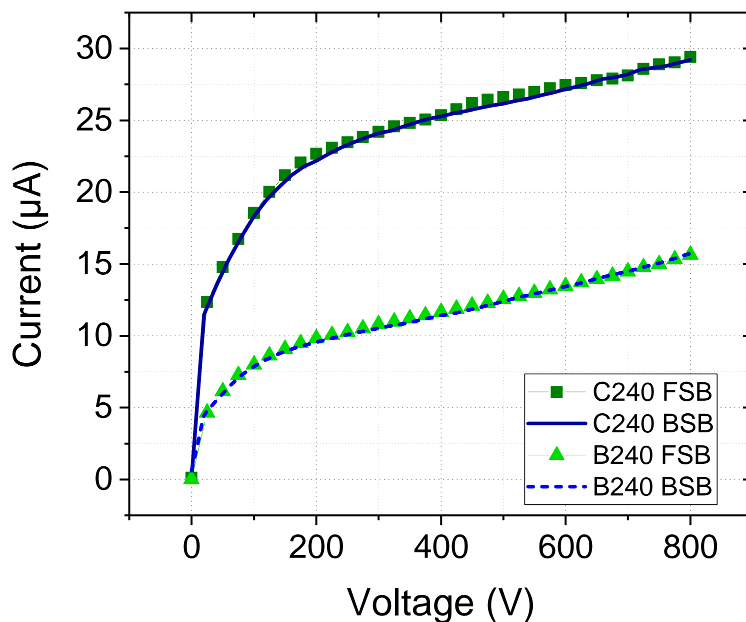

Figure 3. Comparison of front-side-biased and back-side-biased IV measurements performed on two mini sensors of differing size.

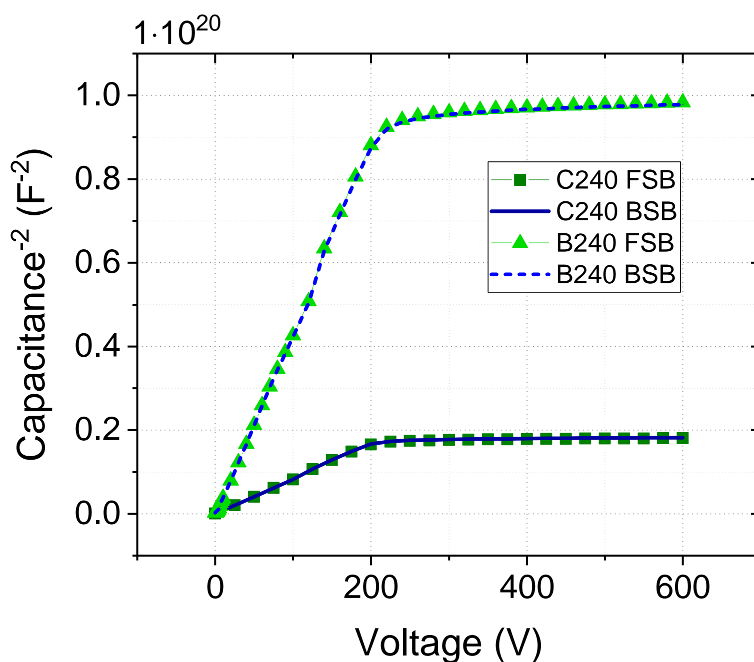

Figure 4. Comparison of front-side-biased and back-side-biased CV measurements performed on two mini sensors of differing size.

2018 JINST 13 P11007

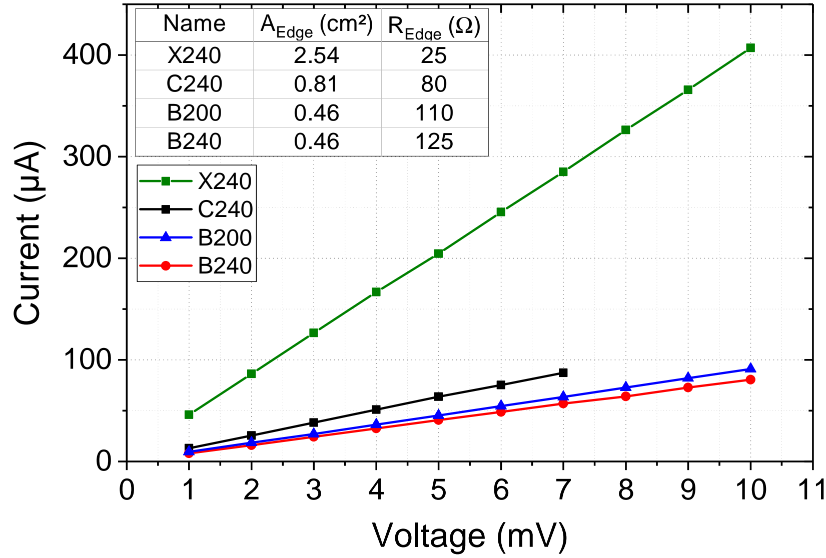

Figure 5. Illustration of four edge resistivity measurements.

5 Impact of edge dimensions

As depicted in figure 1, edge resistivity measurements were performed by applying LV ramps between edge ring and back-side. Voltage ramps were performed in steps of millivolts up to 1 V at room temperature. Depending on the size of A_{edge} and the bulk resistivity of the sample, a few millivolts suffice to induce currents of several 100 µA. For these measurements the bias voltage was $V_{\text{bias}} = 0$ V. The results shown in figure 5 reveal that the IV characteristic of the edge before irradiation follows Ohm's law. The resistance is calculated by using Equation (3.11). One can see that a larger edge dimension leads to lower resistances. The results also support the assumption that not the physical thickness, but only the active thickness contributes to ρ (comparison of B200 and B240). However, the difference in resistance is rather small and might seem close to the expected uncertainties. On the other hand, the difference is expected to be small. The ratios of active thickness and edge resistance are comparable:

$$\frac{L_{\text{B200}}}{L_{\text{B240}}} = 0.83 \approx \frac{R_{\text{B200}}}{R_{\text{B240}}} = 0.88\,. \tag{5.1}$$

To additionally validate this assumption, the resistance of the edge region was simulated in TCAD with a typical bulk resistivity for HPK material of 3 kΩcm. An active thickness of 200 µm results in a resistance of 113 Ω, while a thickness of 240 µm yields a resistance of 137 Ω. Since the resistivity is a parameter that can not be set directly in the simulation, one has to tune the doping concentration of the simulated device.

As a next step, one can compare the resistivity obtained by edge resistivity measurements, ρ_{ER}, with the resistivity ρ_{CV}, which is taken from CV measurements on diodes of the respective material. The capacitance increases with voltage and saturates as soon as the bulk is fully depleted. The knee of the CV curve determines the full depletion voltage. The resistivity is derived according

2018 JINST 13 P11007

Table 3. Mean resistivities for different materials resulting from CV measurements on diodes [9] and edge resistivity measurements.

Material	ρ_{ER} (kΩcm)	ρ_{CV} (kΩcm)	ρ_{ER}/ρ_{CV}
240 µm, ddFZ (HPK)	2.7 ± 0.4	3.0 ± 0.1	0.90 ± 0.13
200 µm, ddFZ (HPK)	2.7 ± 0.5	3.3 ± 0.1	0.81 ± 0.12
200 µm, FZ (IFX)	6.3 ± 0.6	6.5 ± 0.3	0.97 ± 0.05

to Equation (3.6). A summary of those results is given in table 3. The values are comparable. The highest deviation is observed for 200 µm ddFZ material.

The variations between sensors indicate that, in practice, the resistivity is not a material constant. It can vary among wafers of the same production batch and even among sensors of a single wafer. The uncertainty of the active thickness ΔL is given by the manufacturer, which is about 5% ($\sim$ 10 µm) and contributes as well to the variations of ρ. The fitting error ΔR is negligible. The deviation between ρ_{ER} and ρ_{CV} is higher for HPK than for IFX material. It is 10% for 240 µm and 19% for 200 µm ddFZ samples, whereas thinned IFX samples show a deviation of only 3% (table 3). This is most likely a consequence of the deep diffused processing. The knee of the doping profile in the transition region becomes milder with thicker backside implantation. Hence, V_{fd} and the active thickness, L, become less well-defined.

6 Bias voltage dependency

Edge resistivity measurements were also performed with $V_{bias} > 0$ V to examine the impact of bulk depletion. The results are shown in figure 6. The dashed line represents a simulation of an IFX sensor with a charge density $N_{ox} = 2 \cdot 10^{10}$ cm^{-2} at the Si-SiO$_2$ interface. The solid lines represent measurements up to a bias voltage of 200 V. The simulated device was tuned to the red-lined D200 sensor. Tuning N_{ox} changed the slope of the curve, which was not neccessary since the default value yielded the desired result. Tuning N is the only possibility to set the resistivity and adjust the resistance for the simulated device. Tuning this parameter seems valid regarding the variations among the measured samples. The bias voltage dependence itself, which is the main focus of this simulation, originates from the default device simulation. The simulated and the experimental results coincide and indicate a proportionality between R_{edge} and V_{bias}:

$$R_{edge} \sim V_{bias} \, . \tag{6.1}$$

The resistances of the measured IFX samples vary within 10%. Thickness variations as discussed in the previous section as well as temperature variations (section 7) are responsible for this.

The relation given by Equation (6.1) is a result of a phenomenon that we call Space Charge Region Constriction (SCRC). It can be explained best by visualizing the spread of the space charge distribution. Figure 7 shows the extent of these distributions for bias voltages of 10 V, 200 V, and 500 V. They extend from the bias ring towards backplane and edge ring. The dimension of the un-depleted region beneath the edge ring is dependent on the width of the depletion region. It is clearly

2018 JINST 13 P11007

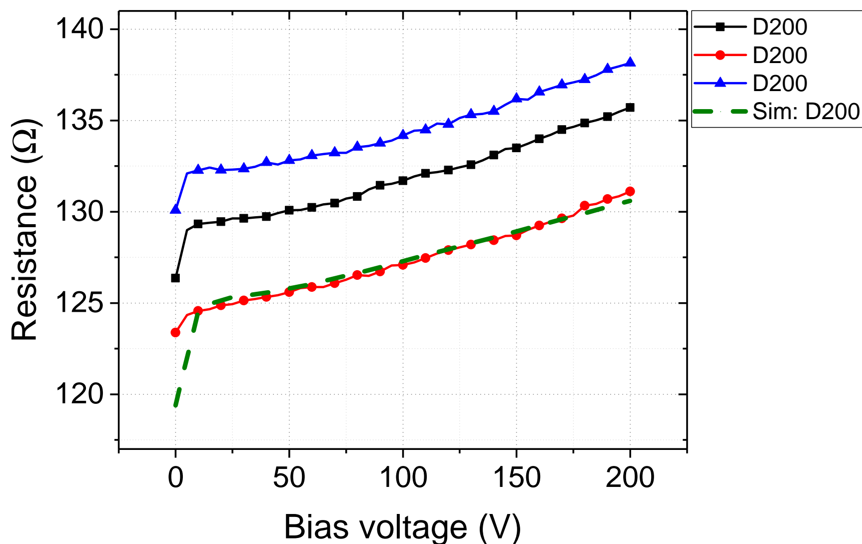

Figure 6. Resistance over bias voltage for IFX sensors. The markers represent experimentally found values on three different sensors of the same type, while full lines are drawn to guide the eye. Simulated results are depicted as a dashed line. The plot indicates that R_{edge} grows with increasing bias voltage.

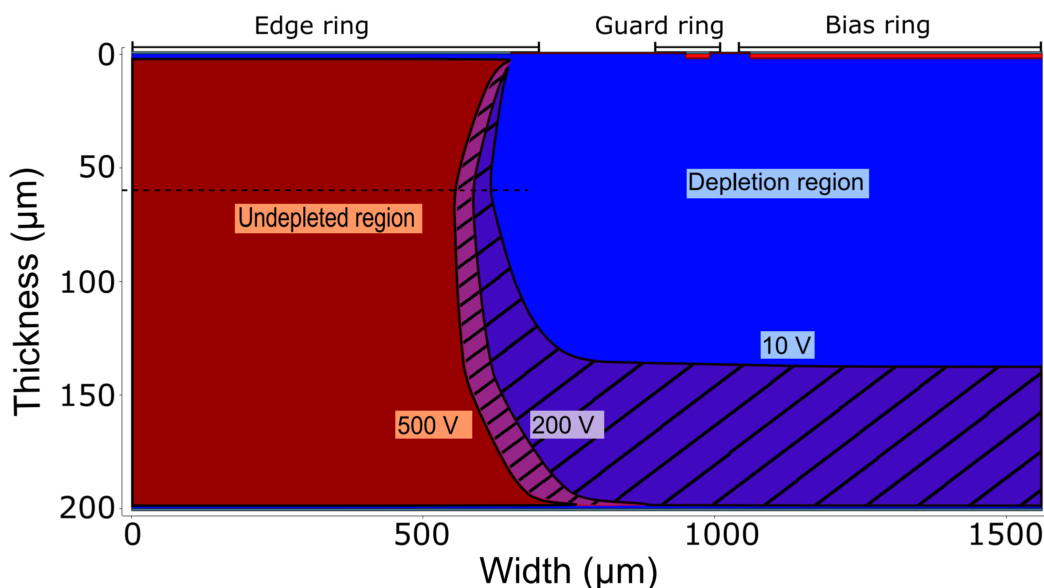

Figure 7. Simulation of the depletion volume for different bias voltages, namely 10 V (blue), 200 V (violet, lines with full spacing), and 500 V (magenta, lines with half spacing). The red region is the undepleted region. With increasing bias voltage the undepleted region underneath the edge ring becomes smaller.

visible that the constriction of the edge region progresses as the bias voltage increases. As indicated by the black dashed line, the constriction turns out to be most prominent at $L = 60$ µm (distance from

2018 JINST 13 P11007

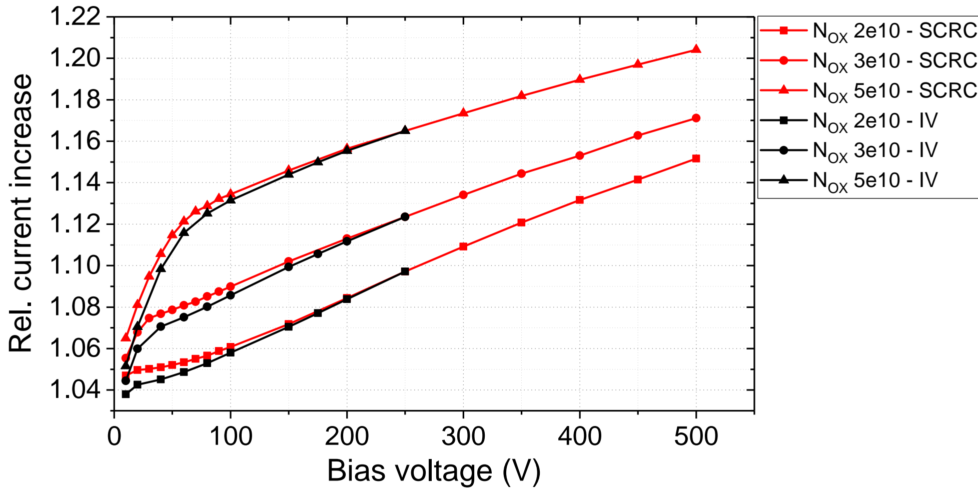

Figure 8. Relative increase of the current as a function of the bias voltage for different values of N_{ox}. The plot summarizes and compares the results of two methods that were used to simulate the impact of V_{bias} on R_{edge}. Red lines represent the outcome of the space charge region constriction method (SCRC). Black lines represent the characteristic gained by simulating the current through the edge and using Ohm's law.

the front-side). The SCRC translates into an effective reduction of the edge width and therefore A_{edge}. Since R_{edge} is inversely proportional to A_{edge} (Equation (3.11)), this results in an increasing resistance. Taking this into account, the SCRC approach models the relative increase of the resistance using the simulated constriction length for different bias voltages and the material resistivity.

For verification, the results of the SCRC simulation can be compared to the second, more straight forward method that was already applied in figure 6: simulating an edge resistivity measurement to obtain the current through the edge, I_{edge}, for different voltages and calculating R_{edge}. The comparison of both methods is shown in figure 8. It illustrates the relative current increase (normalized to a bias voltage of 250 V) as a function of the bias voltage for different N_{ox}. For voltages smaller than 10 V the SCRC approach cannot be used to deduce the resistance, because the depletion region does not extend into the edge region. The offset between the two methods at lower voltages in figure 8 corresponds to a width variation of the SCRC of less than 10 µm, which is also the mesh size used for the simulation. This is negligible compared to the total edge width of 650 µm. To conclude, both methods produce qualitatively similar results that resemble the experimental findings.

7 Temperature dependence before irradiation

The results of edge resistivity measurements between −20 °C and +20 °C are presented in figure 9 and are in agreement with theoretical evaluations presented in section 3. A temperature difference of 40 °C results in a resistance growth of 36%. Fits were made to be able to numerically evaluate the temperature dependence of the resistivity:

$$R = R_0 + R_1 \cdot T^a \,. \tag{7.1}$$

2018 JINST 13 P11007

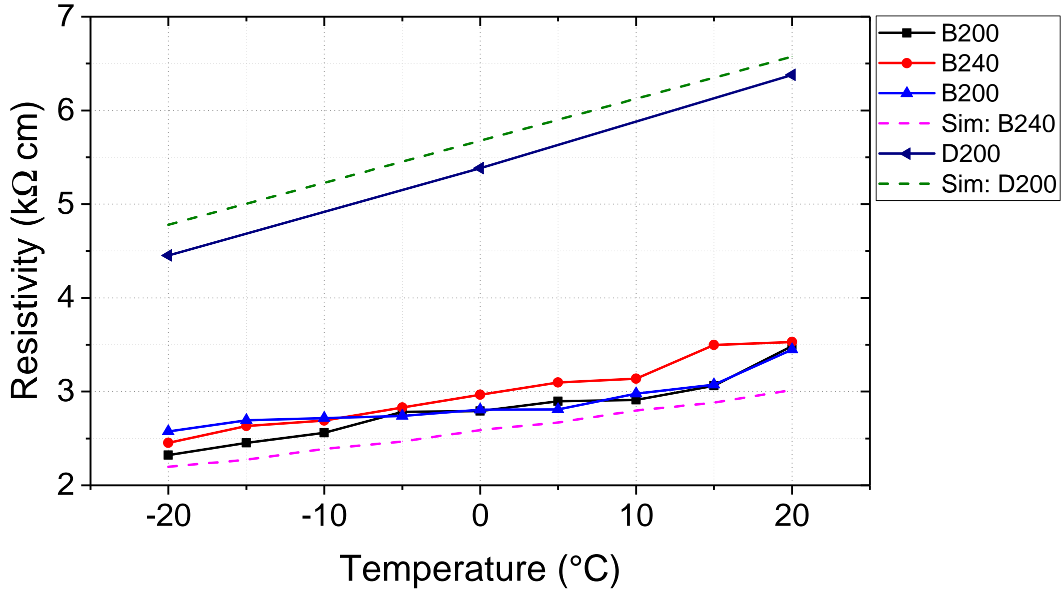

Figure 9. Edge resistivity measurements as a function of temperature between −20 °C and +20 °C. A bias voltage of $V_{\text{bias}} = 0\,\text{V}$ was chosen because the impact of V_{bias} has already been discussed in the previous section. The measurements indicate the expected characteristics described in Equation (3.1) and Relation (3.10).

Table 4. Fit parameters regarding Equation (7.1) with $a = 2.42$ and the data presented in figure 9. The temperature values were converted from °C to K.

Sensor name	R_0 (kΩ cm)	R_1 (kΩ cm $\text{K}^{-2.42}$)
B200 (black)	46 ± 305	0.0035 ± 0.00035
B240	−61 ± 181	0.0039 ± 0.00023
B200 (blue)	880 ± 331	0.0025 ± 0.00042
B240 Simulation	270 ± 33	0.0029 ± 0.00004
D200	−59 ± 59	0.0069 ± 0.00008
D200 Simulation	585 ± 154	0.0064 ± 0.00019

The curves should follow a T^a-characteristic as postulated by theory ($a > 0$). The fact that the shape of the plotted curves in figure 9 does not resemble this characteristic (they appear to be rather linear) is a consequence of the relatively small temperature range. Therefore, a quantitative derivation of the exponent a is not possible without obtaining large errors. The fit parameters listed in table 4 were calculated using the expected value of $a = 2.42$ according to Relation (3.10). The comparability of the fit results supports the theoretical assumptions.

2018 JINST 13 P11007

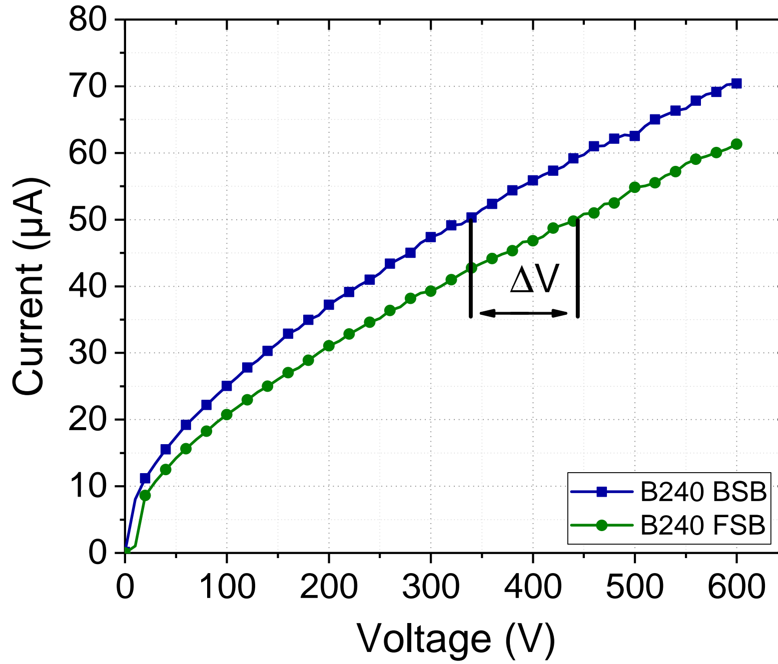

Figure 10. Leakage current comparison of an irradiated sensor irradiated with a fluence of $1 \cdot 10^{15}$ $\mathrm{n_{eq}cm^{-2}}$ and operated via FSB and BSB at −20 °C. The difference between the curves is clearly observable at this fluence and is a result of a high R_{edge} after irradiation.

8 Impact of irradiation

As mentioned in section 4, one can observe no significant difference between FSB and BSB measurements before irradiation. However, the situation changes after irradiation. Figure 10 shows the results of a front-side-biased and back-side-biased IV measurement of the same sensor, meaning that material properties and measurement parameters are identical. One can clearly observe a difference between FSB and BSB. Moreover, this characteristic turns out to be reversible. Changing the biasing scheme always yields the same result. The difference can therefore only originate from a lowered effective bias voltage V_{eff} as a consequence of a non-negligible voltage drop ΔV. The value of ΔV can be calculated from the shift of those two curves at a fixed leakage current value. At 50 µA this is about 100 V. On the other hand, if R_{edge} is known from edge resistivity measurements, one can calculate ΔV by using R_{edge} and the sensor's leakage current I:

$$\Delta V = R_{\mathrm{edge}} \cdot I \,, \tag{8.1}$$

where both R_{edge} and I are proportional to fluence. Since ΔV depends on the edge resistance of a sensor, this can only lead to the conclusion that the resistivity is significantly increased after irradiation. The increase of ρ is supported by edge resistivity measurements shown in figure 11. It saturates between 10 and 100 MΩ cm for fluences above $6 \cdot 10^{14}$ $\mathrm{n_{eq}cm^{-2}}$. Due to the increased resistivity, it was no longer possible to produce currents comparable to those before irradiation with

2018 JINST 13 P11007

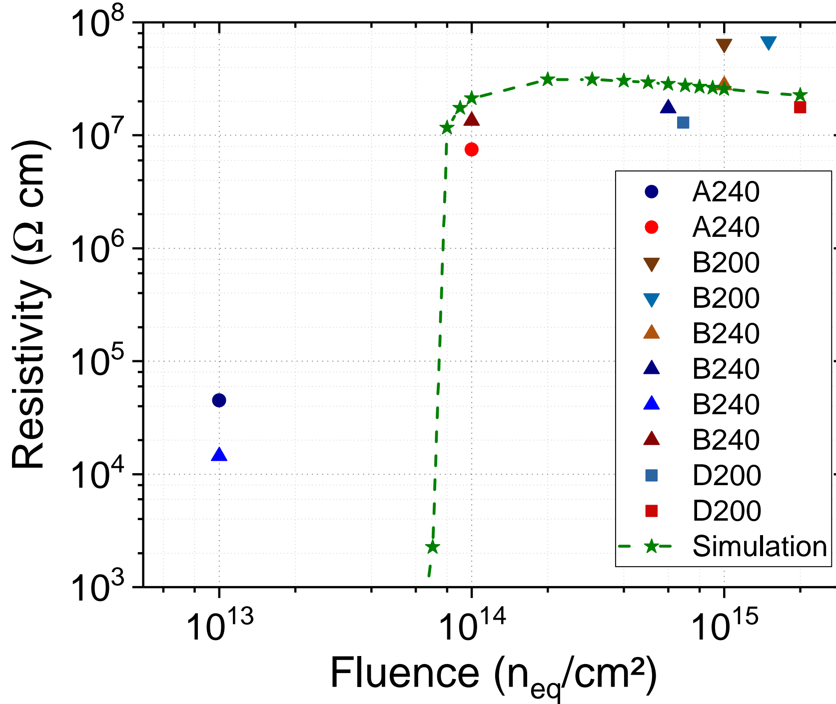

Figure 11. Extracted resistivity ρ from edge resistivity measurements on irradiated mini sensors for different fluences at a temperature of −20 °C. The edge resistivity of the measured samples before irradiation was between 3 and 6 kΩcm. It increases by several orders of magnitude and starts to saturate at a fluence of $1 \cdot 10^{14}\,n_{eq}cm^{-2}$.

voltage ramps up to 1 V. Depending on the size and the fluence of the sensor, one had to apply 50 V or more between edge ring and back-side. The bias voltage was usually kept at $V_{bias} = 0$ V. Since the contribution of SCRC is less than 1 kΩ cm, it is negligible after irradiation. The fitting errors are larger than they were before irradiation since the IV characteristic is not exactly linear for lower currents. This results in an uncertainty of ρ of about 5%.

In ref. [19] measurements on simple silicon resistors with resistivities between 400 and 4500 Ω cm performed at room temperature and after neutron irradiation with similar fluences reported that the resistivity saturated at a value of about 300 kΩ cm. This slightly exceeds the theoretically calculated intrinsic resistivity of silicon at room temperature of 230 kΩ cm [13]. Simulations presented in figure 12 reveal that the hole density decreases after irradiation. As stated by Equation (3.1), a reduction of the sum of p and n leads to an increase of the resistivity of approximately the same order. For a fluence of $6 \cdot 10^{14}\,n_{eq}cm^{-2}$ the decrease is about two orders of magnitude at +20 °C which correlates with the increase of resistivity presented in ref. [19]. At −20 °C the decrease is about four orders of magnitude which coincides with the results shown in figure 11. Furthermore, the saturation close to the intrinsic value at room temperature and the one seen in our measurements at −20 °C for high fluences can be explained by the convergence of electron and hole density. In an intrinsic semiconductor p and n are equal. An increase or decrease

2018 JINST 13 P11007

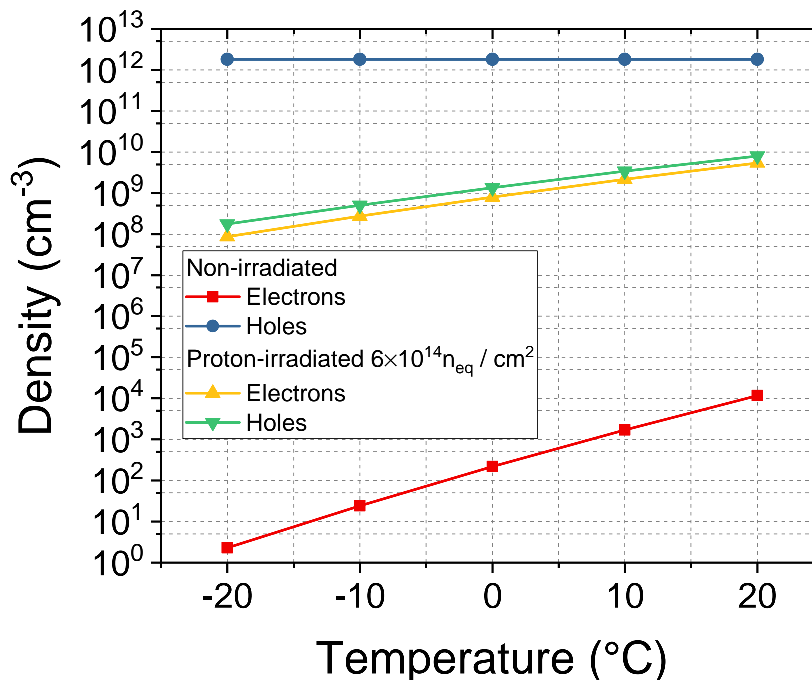

Figure 12. Simulation of the electron and hole density of the center of the edge region for temperatures between −20 °C and +20 °C before and after irradiation.

of both quantities at the same time is forbidden by the mass action law, which yields the intrinsic resistivity as the theoretical limit of ρ. Additional contributions to the resistivtiy as seen in both studies might be related to a decrease of mobility due to defect clustering [19] or trapping.

The carrier mobility is the driving factor of the resistivity vs. temperature characteristic before irradiation. After irradiation, however, the characteristic is dominated by the temperature dependency of the hole and electron concentration. The result is an inverted temperature dependency of the resistivity compared to the one before irradiation. Equation (3.4) shows that the intrinsic carrier density n_{i} follows a $T^{\frac{2}{3}}$-characteristic which indicates a proportionality between ρ and $T^{-\frac{2}{3}}$. Even though we are investigating extrinsic material, the curves seem to follow that trend. This is shown in figure 13 for resistivity measurements after irradiation between −20 °C to +20 °C. Therefore, Equation (3.4) was used as a basis in order to fit the data points:

$$\rho = \rho_0 \cdot T^a \cdot \exp\left(\frac{E_{\mathrm{g}}}{2kT}\right). \tag{8.2}$$

Similar to the fit in section 7, the temperature range is too small to fit the interesting parameters without receiving large errors, which are the exponent a and the bandgap energy E_g. Therefore both values are fixed to the expected values of $a = -1.5$ and $E_g = 1.12\,\mathrm{eV}$. The remaining parameters are summarized in table 5. The temperature is converted from °C to K.

Simulated results of the resistivity are both included in figure 11 and figure 13. Measurements were performed under the same frame conditions. The data show that a temperature variation of 40 °C leads to a resistance change of almost 600% for A200 ($\Phi = 1 \cdot 10^{13}\,\mathrm{n_{eq}cm^{-2}}$). For B200

2018 JINST 13 P11007

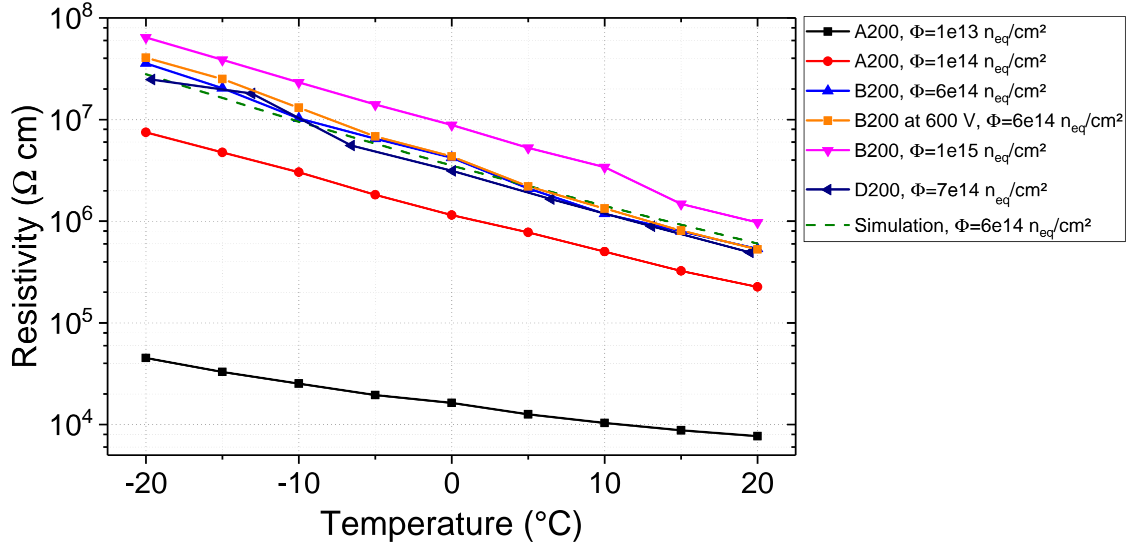

Figure 13. Edge resistivity measurements of irradiated sensors for temperatures between −20 °C and +20 °C at $V_{\text{bias}} = 0$ V. A measurement at $V_{\text{bias}} = 600$ V was added to confirm the negligible impact of the bias voltage after irradiation. The plot indicates that ρ is inversely proportional to temperature.

Table 5. Summary of fit parameters regarding Equation (8.2) and the data presented in figure 13 for $V_{\text{bias}} = 0$.

Φ ($n_{eq}cm^{-2}$)	Sensor name	ρ_0 ($\Omega\,$cm$\,K^{1.5}$)
$1 \cdot 10^{13}$	A200	0.0015 ± 0.00017
$1 \cdot 10^{14}$	A200	0.2214 ± 0.00379
$6 \cdot 10^{14}$	B200	0.9884 ± 0.02388
$1 \cdot 10^{15}$	B200	1.8496 ± 0.01054
$1 \cdot 10^{15}$	D200	0.7920 ± 0.05459

($\Phi = 1 \cdot 10^{15}$ $n_{eq}cm^{-2}$) it is beyond 6600%. This equates to the two orders of magnitude predicted by simulations. The underlying radiation damage model for those simulations includes defect removal and generation mechanisms that are expected to be mainly responsible for the shifts in electron and hole density. By adding more and more defects to the device, the charge carrier concentrations become similar and approach the intrinsic value. A simplified geometry was used for these simulations, where two highly doped p-type implants sandwich a p-type silicon bulk. This configuration corresponds to the edge region. The radiation model is known to work only in a fluence region between $1 \cdot 10^{14}$ $n_{eq}cm^{-2}$ and $1 \cdot 10^{15}$ $n_{eq}cm^{-2}$. Therefore, simulated data below $1 \cdot 10^{14}$ $n_{eq}cm^{-2}$ are not expected to reproduce experimental results. Nevertheless, it provides results which indicate the increase and the saturation of the resistivity as well as the inverted temperature dependence and the simulated values follow the experimental results within the model range of validity.

2018 JINST 13 P11007

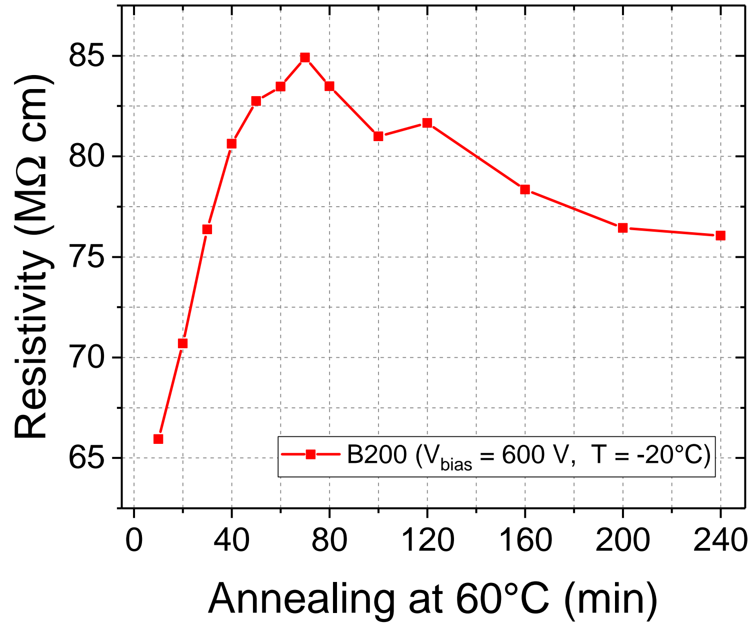

Figure 14. Measured resistivity of a B200 sensor at −20 °C irradiated to a fluence of $6 \cdot 10^{14}$ $n_{eq}cm^{-2}$ with 23 MeV protons, as a function of the annealing time at 60 °C.

9 Annealing effects

This section discusses the impact of annealing on the edge resistivity. For this purpose, edge resistivity measurements were performed on a B200 sensor irradiated to a fluence of $6 \cdot 10^{14}$ $n_{eq}cm^{-2}$. In particular, ρ was measured at different bias voltages and for different annealing times. The temperature during the measurement was −20 °C. Annealing steps ranged from 0 min to 240 min at 60 °C. The results are shown in figure 14. The maximum of the curve is located at the 60 min mark at about 85 MΩ cm. Further annealing results in a decrease of ρ. The edge resistivity of the unannealed sensor was about 45 MΩ cm. Therefore, the relative increase of the resistivity in the first 60 min of annealing is about 88%. The relative decrease from the maximum to the last measurement step at 240 min is about 11%. The uncertainty of the measured values is about 5% as mentioned in section 8. The measurement at V_{bias} = 600 V was chosen because it yielded the smoothest curve. The presented characteristic of the resistivity is independent of the applied bias voltage.

As claimed by ref. [20], the first 80 min of annealing at 60 °C are considered beneficial for the operation of a silicon sensor. During beneficial annealing the acceptor concentration and therefore $|N_{eff}|$ decreases. The observed increase of resistivity with annealing time as a consequence of decreasing $|N_{eff}|$ is described by Equation (3.5). In this case, reverse annealing started between the 60 min and 80 min step. Similar measurements on irradiated silicon resistors were presented in ref. [21]. The results followed the same characteristic.

Figure 15 shows a TCAD simulation of the edge resistivity for different acceptor and donor trap concentrations (defects that undergo annealing). The acceptor (or donor) trap concentration

2018 JINST 13 P11007

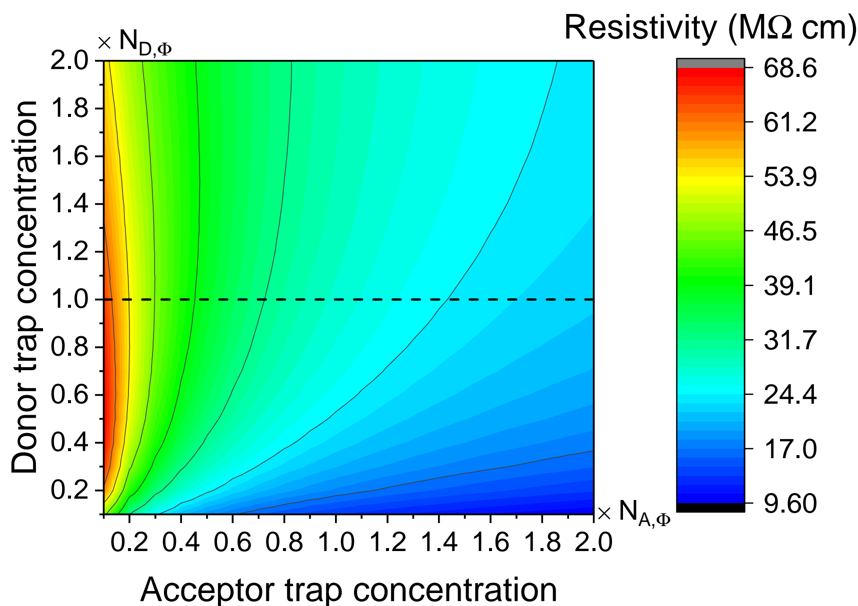

Figure 15. Simulation of the edge resistivity for varying acceptor and donor trap concentrations. $N_{A,\Phi}$ and $N_{D,\Phi}$ represent the acceptor and donor trap concentrations at a fluence of $6.82 \cdot 10^{14}\,n_{eq}cm^{-2}$ according to the irradiation model used in this work. Decreasing the acceptor trap concentration and hence the effective acceptor concentration increases the resistivity, as is expected from beneficial annealing.

in the TCAD model is the defect concentration, which effectively behaves like the acceptor (or donor) concentration. More acceptor traps in the TCAD model mean effectively more acceptors in the bulk. A simplified structure of 200 µm thick p-type bulk with a high p-type implantation on both sides for the two contacts is used to simulate the edge ring. To approximately model the effects of annealing, the acceptor and donor trap concentrations $N_{A,\Phi}$ and $N_{D,\Phi}$ for a fluence of $6 \cdot 10^{14}\,n_{eq}cm^{-2}$ are varied. Along the black dotted line in figure 15 one can see the change in resistivity for different $N_{A,\Phi}$. The simulation confirms that decreasing acceptor concentration leads to an increase of the resistivity. It should be noted that a more detailed modelling of the annealing behaviour is far more complex. Changes in the donor trap concentration and the electron and hole capture cross sections need to be considered as well [10].

10 Extrapolation to large sensors

Based on the results presented in previous sections, one can approximate the voltage drop of a large, irradiated sensor by taking into account the measured edge resistivity of a mini sensor. The desired maximal operation voltage of a typical HEP tracking device such as the Phase-2 Outer Tracker of CMS is 600 V. The expected operation temperature of a sensor is about −20 °C. The expected fluence for the detector modules is simulated to be between $3 \cdot 10^{14}\,n_{eq}cm^{-2}$ and $1 \cdot 10^{15}\,n_{eq}cm^{-2}$ for an integrated luminosity of $3000\,fb^{-1}$. A fluence of $6 \cdot 10^{14}\,n_{eq}cm^{-2}$ seems appropriate for this example, since it is roughly the median of those values and was covered by our measurements. The leakage current at this voltage, fluence, and temperature can be approximated by using the damage

2018 JINST 13 P11007

rate α [20] after an annealing of 80 minutes at 60 °C for a typical sensor of 10 cm x 10 cm x 240 µm like X240. This yields roughly 1 mA. The edge resistivity of a similarly irradiated mini sensor (B240, $\Phi = 6 \cdot 10^{14}$ $n_{eq}cm^{-2}$) is about 17.3 MΩ cm. Considering the dimensions of X240, one finds the edge resistivity to be about 166 kΩ. Since leakage current equates to the current that flows through the edge of a front-side-biased sensor, one can calculate ΔV by using Equation (8.1). According to these assumptions and given parameters, the voltage drop would be 158 V. Multiplying this value with the expected leakage current yields an additional power consumption of 0.15 W per sensor. The CMS Outer Tracker for example consists of roughly 26 000 strip sensors. The additional power consumption would then total 3900 W. More importantly, the additional bias voltage that is necessary to deplete the sensor would exceed the high voltage robustness of the module design [12]. These disadvantages cannot be outweighed by the benefits of FSB and therefore disqualify FSB as a biasing concept for detectors underlying the mentioned frame conditions. However, reducing the fluence in this calculation to $1 \cdot 10^{13}$ $n_{eq}cm^{-2}$ would result in a voltage drop of less than 1 V and a negligible additional power consumption. Such a magnitude would correspond to the expected fluence in the LHCb experiment [22]. The disadvantages could also be minimized by reducing the sensor dimensions, the thickness and the resistivity of the material, as well as increasing the edge area or increasing the operation temperature.

11 Summary

Module assembly for large silicon trackers could benefit from FSB due to single-sided procedures. The sensor back-side can be connected via the conductive edge from the top-side. The validity of this biasing scheme was studied by measuring the sensor leakage current, the sensor capacitance and the direct current through the sensor edge of n-in-p silicon strip sensors. Measurements were performed at ETP and HEPHY with different materials on unirradiated and irradiated samples with fluences ranging from $1 \cdot 10^{13}$ $n_{eq}cm^{-2}$ to $2 \cdot 10^{15}$ $n_{eq}cm^{-2}$ and temperatures between −20 °C and +20 °C. The data were interpreted and complemented by simulations. The results can be summarized as follows:

- There is no observable difference between front-side-biased and back-side-biased IV and CV characteristics before irradiation. The voltage drop ΔV is negligible due to a low-ohmic edge resistance.

- The resistor formula is a valid tool to extract the edge resistivity from direct IV measurements through the edge (edge resistivity measurements). The extracted values of the resistivity for the two sensor materials are comparable to the results of CV measurements.

- The edge resistance of unirradiated sensors increases with increasing bias voltage due to a mechanism that we call Space Charge Region Constriction (SCRC). The depletion zone increases with increasing bias voltage. Simulations show that it starts to constrict the edge region even at low voltages. The increasing constriction leads to an increasing edge resistance.

- The edge resistivity is proportional to temperature before irradiation. This is caused by an impaired carrier mobility due to phonon scattering. The expected relation of $\rho \sim T^{2.42}$ could

2018 JINST 13 P11007

be confirmed within the measurement accuracy. In a temperature range from −20 °C to +20 °C the resistance increases about 36%.

- The edge resistivity after irradiation saturates between 10^7 and 10^8 Ω cm for fluences larger than $6 \cdot 10^{14}$ $n_{eq}cm^{-2}$ at a measurement temperature of −20 °C. At room temperature it saturates close to the intrinsic value of silicon of 230 kΩ cm. Simulations targeting the electron and hole density at temperatures between −20 °C to +20 °C before and after irradiation explain these observations. A reduction of the sum of hole and electron density leads to an increase of resistivity of approximately the same order. For high fluences hole and electron density converge, which yields the intrinsic resistivity as the limit. At −20 °C the hole and electron density are reduced by two orders of magnitude which coincides with the additional two orders of magnitude shown by our measurements. The resistivity might be further increased by a small portion due to defect clustering and a reduction of carrier mobility as well as trapping. The temperature dependence of ρ after irradiation is inverted compared to the one before irradiation, since carrier density is proportional to temperature.

- The edge resistivity is impacted by annealing effects. It increases continuously during beneficial annealing. Further annealing leads to a decrease. This is related to the changing level of $|N_{eff}|$ with annealing time.

- The measured values of the edge resistivity of mini sensors can be used to extrapolate ΔV for large sensors as they are used in modern HEP experiments (e.g. 10 cm x 10 cm sensor area). At a fluence of $6 \cdot 10^{14}$ $n_{eq}cm^{-2}$, a temperature of −20 °C and a bias voltage of 600 V this is approximately 158 V. This disadvantage disqualifies FSB as a baising concept for experiments like the CMS Phase-2 Outer Tracker.

Acknowledgments

The sensors were developed and produced in the framework of the CMS Phase-2 Tracker Upgrade activities. The collaboration kindly agreed to let us use the sensors for this study.

The research leading to these results has been co-funded by the European Commission under the Horizon 2020 Research Infrastructures project AIDA-2020, Grant Agreement 654168.

The research leading to these results has received funds from the call "Forschungspartnerschaften" of the Austrian Research Promotion Agency (FFG) under the grant no. 849087.

References

[1] T. Nakayama, S. Arai, K. Hara, M. Shimojima, Y. Ikegami, Y. Iwata et al., *Radiation damage studies of silicon microstrip sensors*, *IEEE Trans. Nuc. Sci.* **47** (2000) 1885.

[2] Hamamatsu Photonics K.K., Japan, http://www.hamamatsu.com.

[3] Infineon Technologies Austria AG, https://www.infineon.com.

[4] T. Bergauer, *Silicon sensor prototypes for the Phase II upgrade of the CMS tracker*, *Nucl. Instrum. Meth.* **A 831** (2016) 161.

[5] Institut für Experimentelle Teilchenphysik, Germany, https://www.etp.kit.edu/.

2018 JINST 13 P11007

[6] Karlsruher Institut für Technologie, Germany, https://www.kit.edu/.

[7] Institut für Hochenergiephysik, Austria, http://www.hephy.at/.

[8] Synopsys Inc., U.S.A., https://www.synopsys.com/silicon/tcad.html.

[9] T. Bergauer, M. Dragicevic, A. König, J. Hacker and U. Bartl, *First thin AC-coupled silicon strip sensors on 8-inch wafers*, *Nucl. Instrum. Meth.* **A 830** (2016) 473.

[10] R. Eber, *Untersuchung neuartiger Sensorkonzepte und Entwicklung eines effektiven Modells der Strahlenschädigung für die Simulation hochbestrahlter Silizium-Teilchendetektoren*, Ph.D. thesis, Karlsruher Institut für Technologie (KIT) (2013).

[11] Zyklotron AG, Germany, http://www.zyklotron-ag.de.

[12] CMS collaboration, *The Phase-2 Upgrade of the CMS Tracker*, Tech. Rep. CERN-LHCC-2017-009, CMS-TDR-014, CERN, Geneva (2017).

[13] S. Sze, *Physics of Semiconductor Devices*, John Wiley & Sons (1981).

[14] F. Hartmann, *Evolution of Silicon Sensor Technology in Particle Physics*, Springer Tracts in Modern Physics, Springer, Berlin Heidelberg (2008).

[15] V. Zeghbroeck, *Principles of Semiconductor Devices and Heterojunctions*, Prentice Hall PTR (2007).

[16] M. Grundmann, *The Physics of Semiconductors: An Introduction Including Nanophysics and Applications*, Springer, Berlin Heidelberg (2010).

[17] G. Lutz, *Semiconductor Radiation Detectors: Device Physics*, Springer, Berlin Heidelberg (2007).

[18] C. Jacoboni, C. Canali, G. Ottaviani and A.A. Quaranta, *A review of some charge transport properties of silicon*, *Solid State Electron.* **20** (1977) 77.

[19] B. Dezillie, Z. Li, V. Eremin, M. Bruzzi, S. Pirollo, S.U. Pandey et al., *Improved neutron radiation hardness for Si detectors: Application of low resistivity starting material and/or manipulation of N(eff) by selective filling of radiation-induced traps at low temperatures*, *IEEE Trans. Nucl. Sci.* **46** (1999) 221.

[20] M. Moll, *Radiation damage in silicon particle detectors: Microscopic defects and macroscopic properties*, Ph.D. thesis, Hamburg University (1999).

[21] Z. Li, *Elevated temperature annealing behaviors of bulk resistivity and space charge density of neutron irradiated silicon detectors and materials*, *Nucl. Instrum. Meth.* **A 368** (1996) 353.

[22] M. Siegler, F. Lehner, M. Needham and O. Steinkamp, *Expected Particle Fluences and Performance of the LHCb Trigger Tracker*, CERN-LHCb-2004-070 (2004).

2018 JINST 13 P11007